Numerical Solution of Space Shuttle Orbiter Flowfield Including Real-Gas Effects

Dinesh K. Prabhu* and J.C. Tannehill†
Iowa State University, Ames, Iowa

The hypersonic, laminar flow around the Space Shuttle Orbiter has been computed for both an ideal gas ($\gamma = 1.2$) and equilibrium air using a real-gas, parabolized Navier-Stokes code. This code employs a generalized coordinate transformation; hence, it places no restrictions on the orientation of the solution surfaces. The initial solution in the nose region was computed using a three-dimensional, real-gas, time-dependent Navier-Stokes code. The thermodynamic and transport properties of equilibrium air were obtained from either approximate curve fits or a table look-up procedure. Numerical results are presented for flight conditions corresponding to the STS-3 trajectory. The computed surface pressures and convective heating rates are compared with data from the STS-3 flight.

Introduction

THE accurate prediction of the flowfield and heating environment around the Space Shuttle Orbiter has been the aim of recent research efforts. Previously, the inviscid flow around the Orbiter has been computed by solving the Euler equations.[1-5] In order to account for viscous effects, the inviscid solutions have been coupled with matching boundary-layer analyses.[6-10] These latter methods have been effective in predicting the thermal environment on the windward side of the Orbiter. The problem of specifying the proper edge conditions in the matching boundary-layer analyses has been avoided by several investigators through the use of viscous shock-layer (VSL) equations.[11-15] Unfortunately, VSL equations cannot be used to predict the flowfield on the leeward side of the Orbiter for high angles of attack because of the cross-flow separation. In addition, an approximate Orbiter geometry is required with this analysis in order to overcome the problems encountered at the wing-fuselage juncture. On the other hand, the "parabolized" Navier-Stokes (PNS) equations have shown great promise in predicting the complete inviscid-viscous flowfield around Shuttle-like bodies[16] as well as more realistic Shuttle body shapes.[17-19] The PNS equations are uniformly valid throughout the shock layer and can be used in regions of large cross-flow separation.

The generalized PNS code developed by Tannehill et al.[20] is ideally suited for the complex flowfield that develops around the leading edge and in the region of the wing-body juncture of the Orbiter. This generalized PNS code accepts the initial solution on any starting surface and lets the solution proceed from one data surface to another without any restriction on the orientation of these surfaces. The only condition that must be met is that the velocity component normal to the solution surface must be supersonic in the inviscid region. This code has been used to make perfect-gas calculations around a realistic Shuttle geometry at angles of attack as high as 30 deg for different freestream Mach numbers.[18]

In the present study, the generalized PNS code has been modified to permit real-gas (equilibrium-air) calculations. Real-gas effects are especially important in predicting the reentry environment around the Shuttle because the high temperatures within the shock layer cause the air to dissociate and ionize, thus invalidating the perfect-gas assumption. Maus et al.[21] have shown that real-gas effects can have a significant influence on the Orbiter aerodynamics. In simulating real-gas flows one requires thermodynamic and transport properties of the gas. For an ideal gas the properties are available in compact analytical expressions. For a real gas, however, such simple expressions are not available. Recently, Balakrishnan et al.[22] and Balakrishnan and Davy[23] have computed the inviscid and viscous flowfields of equilibrium air around the Orbiter nose. They obtained the thermodynamic properties by solving the chemical equilibrium equations and the transport properties using mixture rules. While such an approach is very general and is applicable to any kind of gas mixture, it requires a substantial amount of computer time. For the present study, the thermodynamic and transport properties of equilibrium air were obtained from approximate curve fits or a table look-up procedure. Using this approach the real-gas flow around the Orbiter has been computed for flight conditions corresponding to the STS-3 trajectory. The results of these calculations are compared with data from the STS-3 flight and results from an "effective γ" (i.e., $\gamma = 1.2$) ideal-gas calculation.

Presented as Paper 84-1747 at the AIAA 19th Thermophysics Conference, Snowmass, CO, June 25-28, 1984; submitted March 7, 1985; revision received Sept. 10, 1985.

*Research Assistant, Department of Aerospace Engineering and Computational Fluid Dynamics Center. Member AIAA.

†Professor, Department of Aerospace Engineering; Manager, Computational Fluid Dynamics Center. Associate Fellow AIAA.

Governing Equations

PNS Equations

The PNS equations are obtained from the complete Navier-Stokes equations by neglecting the unsteady terms and the streamwise viscous derivative terms. The equations in nondimensional, strong conservation-law form can be written for a generalized curvilinear coordinate system as

$$\frac{\partial E}{\partial \xi} + \frac{\partial F}{\partial \eta} + \frac{\partial G}{\partial \zeta} = \frac{1}{Re_L}\left(\frac{\partial F_v}{\partial \eta} + \frac{\partial G_v}{\partial \zeta}\right) \tag{1}$$

where the generalized coordinates (ξ,η,ζ) are related to the Cartesian coordinates (x,y,z) through the transformations $\xi = \xi(x,y,z)$, $\eta = \eta(x,y,z)$, and $\zeta = \zeta(x,y,z)$, and the five-component inviscid flux vector E is

$$E = \frac{1}{J}\begin{bmatrix} \rho(u\xi_x + v\xi_y + w\xi_z) \\ \rho u(u\xi_x + v\xi_y + w\xi_z) + \xi_x p \\ \rho v(u\xi_x + v\xi_y + w\xi_z) + \xi_y p \\ \rho w(u\xi_x + v\xi_y + w\xi_z) + \xi_z p \\ (\rho e_t + p)(u\xi_x + v\xi_y + w\xi_z) \end{bmatrix} \tag{2}$$

The other inviscid flux vectors $\boldsymbol{F}$ and $\boldsymbol{G}$ can be obtained by substituting η for ξ and ζ for ξ, respectively, in Eq. (2). The viscous flux vector $\boldsymbol{F}_v$ is

$$\boldsymbol{F}_v = \frac{1}{J}\begin{bmatrix} 0 \\ \mu(\ell_1 u_\eta + \ell_4 v_\eta + \ell_5 w_\eta) \\ \mu(\ell_4 u_\eta + \ell_2 v_\eta + \ell_6 w_\eta) \\ \mu(\ell_5 u_\eta + \ell_6 v_\eta + \ell_3 w_\eta) \\ \mu(\ell_1 u + \ell_4 v + \ell_5 w)u_\eta \\ +\mu(\ell_4 u + \ell_2 v + \ell_6 w)v_\eta \\ +\mu(\ell_5 u + \ell_6 v + \ell_3 w)w_\eta \\ +\dfrac{k}{(\gamma_\infty - 1)M_\infty^2 Pr_\infty} T_\eta \end{bmatrix} \tag{3}$$

where

$$\ell_1 = \frac{4}{3}\eta_x^2 + \eta_y^2 + \eta_z^2 \qquad \ell_5 = \frac{\eta_x \eta_z}{3}$$

$$\ell_2 = \eta_x^2 + \frac{4}{3}\eta_y^2 + \eta_z^2 \qquad \ell_6 = \frac{\eta_y \eta_z}{3}$$

$$\ell_3 = \eta_x^2 + \eta_y^2 + \frac{4}{3}\eta_z^2 \qquad \ell_7 = \eta_x^2 + \eta_y^2 + \eta_z^2$$

$$\ell_4 = \frac{\eta_x \eta_y}{3} \tag{4}$$

The viscous flux vector $\boldsymbol{G}_v$ can be obtained by substituting ζ for η in Eqs. (3) and (4).

The specific total energy can be written as the sum of the specific internal energy and kinetic energy, i.e.,

$$e_t = e + (u^2 + v^2 + w^2)/2 \tag{5}$$

In addition to the above flux vectors, another vector $\boldsymbol{U}$ can be defined as

$$\boldsymbol{U} = U/J = [\rho, \rho u, \rho v, \rho w, \rho e_t]^T/J \tag{6}$$

The details of the spatial coordinate transformation, the expressions for the metrics, and the Jacobian J of the transformation can be found in Refs. 20 and 24.

The quantities appearing in Eqs. (1-6) have been nondimensionalized (dimensional quantities are indicated by a tilde) as follows:

$$x = \tilde{x}/\tilde{L}, \qquad y = \tilde{y}/\tilde{L}, \qquad z = \tilde{z}/\tilde{L}$$

$$u = \tilde{u}/\tilde{V}_\infty, \qquad v = \tilde{v}/\tilde{V}_\infty, \qquad w = \tilde{w}/\tilde{V}_\infty$$

$$\rho = \tilde{\rho}/\tilde{\rho}_\infty, \qquad p = \tilde{p}/\tilde{\rho}_\infty \tilde{V}_\infty^2, \qquad T = \tilde{T}/\tilde{T}_\infty$$

$$e = \tilde{e}/\tilde{V}_\infty^2, \qquad \mu = \tilde{\mu}/\tilde{\mu}_\infty, \qquad k = \tilde{k}/\tilde{k}_\infty \tag{7}$$

where $\tilde{L}$ is the characteristic or reference length; and $\tilde{\rho}_\infty$, $\tilde{V}_\infty$, $\tilde{T}_\infty$, $\tilde{\mu}_\infty$, and $\tilde{k}_\infty$ are the freestream density, velocity, temperature, coefficient of viscosity, and the coefficient of thermal conductivity, respectively. The other dimensionless parameters in Eqs. (1-6) are the Reynolds number Re_L, the freestream Mach number M_∞, and the freestream Prandtl number Pr_∞. These parameters are defined as

$$Re_L = \tilde{\rho}_\infty \tilde{V}_\infty \tilde{L}/\tilde{\mu}_\infty \tag{8}$$

$$Pr_\infty = \tilde{\mu}_\infty \gamma_\infty \tilde{R}_\infty/(\gamma_\infty - 1)\tilde{k}_\infty \tag{9}$$

$$M_\infty = \tilde{V}_\infty/\tilde{a}_\infty \tag{10}$$

where $\tilde{a}_\infty$ is the freesteam speed of sound, γ_∞ the freestream ratio of specific heats, and $\tilde{R}_\infty$ the freestream gas constant.

Thermodynamic and Transport Properties

In order to close the above system of PNS equations, relations between the thermodynamic variables are required along with expressions for the transport properties, μ and k. The relations between the thermodynamic variables depend on the type of gas model.

At this point two useful quantities can be defined:

$$\bar{\gamma} = h/e \tag{11}$$

$$\beta = \gamma_\infty M_\infty^2 p/\rho T \tag{12}$$

The first quantity, which is the ratio of the specific static enthalpy to the specific internal energy, is analogous to the ratio of specific heats. For an ideal gas, $\bar{\gamma}$ and γ are identical if h and e are referenced to 0 K. The second quantity, which is the compressibility of the gas, is a measure of the deviation of a gas from ideal behavior. The factor $\gamma_\infty M_\infty^2$ appears in the definition of compressibility because of the nondimensionalization of the variables.

Ideal Gas

For an ideal gas (i.e., a gas that is both calorically and thermally perfect) the following relations are valid:

$$\bar{\gamma} = \gamma_\infty = \text{const} = \gamma \tag{13}$$

$$\beta = 1 \Rightarrow T = \gamma M_\infty^2 p/\rho \tag{14}$$

$$p = (\gamma - 1)\rho e \tag{15}$$

The transport properties are obtained from simple expressions. The nondimensional coefficient of viscosity, μ, is calculated from Sutherland's law

$$\mu = (T)^{3/2}(1 + C)/(T + C) \tag{16}$$

where $C = 110.4\ \text{K}/\tilde{T}_\infty$ for air. Assuming the Prandtl number to remain constant over the entire flowfield, the nondimensional coefficient of thermal conductivity, k, is given by

$$k = \mu \tag{17}$$

Real Gas

For the present computations the real gas is assumed to be air in chemical equilibrium. For equilibrium air, the thermodynamic and transport properties are available in the form of approximate curve fits designed especially for use with finite difference methods.

These approximate curve fits for the thermodynamic properties were developed by Tannehill and associates.[25,26] They provide the following correlations:

$$\tilde{p} = \tilde{p}(\tilde{e}, \tilde{\rho}), \quad \tilde{a} = \tilde{a}(\tilde{e}, \tilde{\rho}), \quad \tilde{T} = \tilde{T}(\tilde{e}, \tilde{\rho})$$

$$\tilde{h} = \tilde{h}(\tilde{p}, \tilde{\rho}), \quad \tilde{T} = \tilde{T}(\tilde{p}, \tilde{\rho}) \tag{18}$$

In addition to these curve fits, Tannehill and Mohling[25] have modified the table look-up procedure employed by the NASA Ames RGAS program[27] to permit $\tilde{e}$ and $\tilde{\rho}$ to be used as independent variables. The curve fits and table look-up procedure are valid for temperatures up to 25,000 K and densities from 10^{-7} to 10^3 Amagats – ratio of density to reference density (ρ/ρ_0). The table look-up procedure is more accurate than the curve fits but requires substantially more computer time.

The curve fits for the transport properties were developed by Vigneron[28] and include the following correlations:

$$\tilde{\mu} = \tilde{\mu}(\tilde{e}, \tilde{\rho}), \qquad \tilde{k} = \tilde{k}(\tilde{e}, \tilde{\rho}) \tag{19}$$

These curve fits are valid for temperatures up to 15,000 K and pressures from 10^{-4} to 10^{2} atm.

The correlation $\tilde{p}=\tilde{p}(\tilde{e},\tilde{\rho})$ is obtained from a curve fit for

$$\tilde{\gamma}=\tilde{\gamma}(\tilde{e},\tilde{\rho}) \tag{20}$$

in conjunction with

$$\tilde{p}=(\tilde{\gamma}-1)\tilde{\rho}\tilde{e} \tag{21}$$

Upon nondimensionalizing Eq. (21) and combining with Eq. (12), the nondimensional temperature can be written as

$$T=\gamma_\infty M_\infty^2\frac{(\tilde{\gamma}-1)}{\beta}e \tag{22}$$

Streamwise Pressure Gradient

The PNS equations, given by the above system of equations, are hyperbolic-parabolic in the ξ direction if the inviscid region of the flowfield is completely supersonic, if there is no streamwise flow separation within the domain of interest, and if the steamwise pressure gradient, $\partial p/\partial\xi$, in the subsonic portion of the boundary layer is treated in such a manner as to suppress departure or exponentially growing solutions.

There are a number of different techniques to suppress the departure solutions associated with the pressure gradient term. The method proposed by Vigneron et al.[29] is used in the present computations. In this method the flux vector E is split into two parts,

$$E=E^*+P \tag{23}$$

where

$$E^*=\frac{1}{J}\begin{bmatrix}\rho(u\xi_x+v\xi_y+w\xi_z)\\ \rho u(u\xi_x+v\xi_y+w\xi_z)+\omega\xi_x p\\ \rho v(u\xi_x+v\xi_y+w\xi_z)+\omega\xi_y p\\ \rho w(u\xi_x+v\xi_y+w\xi_z)+\omega\xi_z p\\ (\rho e_t+p)(u\xi_x+v\xi_y+w\xi_z)\end{bmatrix} \tag{24}$$

and

$$P=(1-\omega)p[0,\xi_x,\xi_y,\xi_z,0]^T/J \tag{25}$$

The factor ω is given by

$$\omega=\sigma\tilde{\gamma}M_\xi^2/[1+(\tilde{\gamma}-1)M_\xi^2], \qquad M_\xi<1$$
$$=1, \qquad M_\xi\geq 1 \tag{26}$$

where

$$M_\xi=(u\xi_x+v\xi_y+w\xi_z)/a(\xi_x^2+\xi_y^2+\xi_z^2)^{1/2} \tag{27}$$

and σ is a safety factor. For the present calculations, the "elliptical" portion of the streamwise pressure gradient, i.e., $\partial P/\partial\xi$, has been ignored in the subsonic region of the boundary layer.

Numerical Solution of Equations

Finite Difference Algorithm

In order to integrate the PNS equations in generalized coordinates, an efficient, noniterative, implicit finite difference scheme developed by Tannehill et al.[20] is used. This algorithm in delta form is

$$\left\{\left(\frac{\partial E^*}{\partial U}\right)+\frac{\theta_1\Delta\xi}{1+\theta_2}\frac{\partial}{\partial\zeta}\left(\frac{\partial G}{\partial U}-\frac{1}{Re_L}\frac{\partial G_v}{\partial U}\right)\right\}\left(\frac{\partial E^*}{\partial U}\right)^{-1}$$
$$\times\left\{\left(\frac{\partial E^*}{\partial U}\right)+\frac{\theta_1\Delta\xi}{1+\theta_2}\frac{\partial}{\partial\eta}\left(\frac{\partial F}{\partial U}-\frac{1}{Re_L}\frac{\partial F_v}{\partial U}\right)\right\}\Delta^i U$$
$$=-\Delta\xi\left(\frac{\partial E^*}{\partial\xi}\right)_U^i-\frac{\Delta\xi}{1+\theta_2}\left\{\frac{\partial}{\partial\eta}\left(F-\frac{F_v}{Re_L}\right)\right.$$
$$\left.+\frac{\partial}{\partial\zeta}\left(G-\frac{G_v}{Re_L}\right)\right\}^i+\frac{\theta_2}{1+\theta_2}\Delta^i E^*-\Delta^i P$$
$$-\frac{\theta_1}{1+\theta_2}(\Delta\xi)^2\left\{\frac{\partial}{\partial\eta}\left[\frac{\partial}{\partial\xi}\left(F-\frac{F_v}{Re_L}\right)_U\right]^i\right.$$
$$\left.+\frac{\partial}{\partial\zeta}\left[\frac{\partial}{\partial\xi}\left(G-\frac{G_v}{Re_L}\right)_U\right]^i\right\} \tag{28}$$

where the superscript i refers to the station $\xi=i\Delta\xi$ and

$$\Delta^i U=U^{i+1}-U^i \tag{29}$$

The complete details of the algorithm can be found in Refs. 20 and 24. For equilibrium air, however, the Jacobians have to be modified because the thermodynamic variables and transport properties are functions of the components of the solution vector. The modified inviscid and viscous Jacobians for a gas in chemical equilibrium are given in Ref. 30.

Boundary Conditions

At every streamwise station the solution surface $\xi=\xi(x,y,z)=\text{const}$ is bounded by 1) the outer bow shock, 2) the inner body surface, and 3) the plane of symmetry for flows without yaw. At the plane of symmetry, reflection boundary conditions are imposed implicitly. Thus, flow symmetry is maintained for the cases without yaw. The outer bow shock is treated as an infinitesimally thin discontinuity obeying laws of conservation of

Mass:

$$\rho_1 V_1=\rho_2 V_2 \tag{30}$$

Momentum:

$$\rho_1 V_1^2+p_1=\rho_2 V_2^2+p_2 \tag{31}$$

Energy:

$$V_1^2/2+h_1=V_2^2/2+h_2 \tag{32}$$

where V_1 and V_2 are velocity components normal to the shock. The subscripts 1 and 2 indicate states ahead of and behind the shock, respectively.

A combination of the mass and momentum conservation equations yields

$$V_1^2=\left(\frac{p_2-p_1}{\rho_1}\right)\left(\frac{1}{1-\rho_1/\rho_2}\right) \tag{33}$$

and a combination of all three conservation equations yields

$$h_2=h_1+\left(\frac{p_2-p_1}{2\rho_1}\right)(1+\rho_1/\rho_2) \tag{34}$$

In the Thomas method of "shock fitting,"[31] the pressure p_2 behind the shock is required. For the present calculations, this

pressure is obtained by a simple one-sided application of the finite difference algorithm.

For equilibrium air, the correlations

$$\tilde{h}_1 = \tilde{h}_1(\tilde{p}_1, \tilde{\rho}_1) \tag{35}$$

and

$$\tilde{h}_2 = \tilde{h}_2(\tilde{p}_2, \tilde{\rho}_2) \tag{36}$$

are readily available in the forms discussed previously for equilibrium air. With these correlations, Eq. (34) becomes an implicit equation for the unknown ρ_2. This equation is solved iteratively by the bisection method. Once ρ_2 is obtained, the velocity V_1 is easily determined from Eq. (33). For an ideal gas, however, such an iterative procedure is not required. Combining the thermodynamic identity

$$h = e + p/\rho \tag{37}$$

with the ideal-gas relations [Eqs. (13) and (15)], Eq. (34) can be simplified to an explicit relation for the unknown ρ_2. Thus, the velocity V_1 can be determined from Eq. (33) without iteration. From this point on the procedure of determining the geometrical quantities at the shock (i.e., shock slope, etc.) is identical to that given in Refs. 20 and 24.

At the wall, the velocity components are set equal to zero and the wall temperature is either specified for the case of an isothermal wall or computed using a one-sided difference approximation for a zero normal temperature gradient when the wall is adiabatic. At the body surface, the pressure is computed by setting the normal pressure gradient equal to zero and using a one-sided difference approximation to represent the derivative. The only unknown that remains at the wall is the density ρ_w. The density is computed from the equilibrium-air correlation

$$\tilde{T}_w = \tilde{T}_w(\tilde{p}_w, \tilde{\rho}_w) \tag{38}$$

using a secant method since a curve fit for $\tilde{\rho}_w = \tilde{\rho}_w(\tilde{T}_w, \tilde{p}_w)$ is not available. For an ideal gas the density is easily determined from Eq. (14).

Orbiter Flowfield Computation

Orbiter Geometry

The Orbiter body surface coordinates are obtained from the geometry package of Rakich and Kutler.[1] This geometry package reproduces the exact Shuttle geometry at 11 different axial locations. Intermediate to these locations, interpolating polynomials are used to produce a smooth geometry that models the actual Shuttle geometry quite closely except near the canopy and in the tail region where the vertical tail and orbital maneuvering system (OMS) pods are omitted. Figure 1 shows the three-dimensional and cross-sectional views of the Orbiter obtained with the above geometry package.

Blunt Nose Starting Solution

The PNS code requires an initial solution surface where the inviscid region of the flowfield is completely supersonic. In the blunt-nose region, however, there is an imbedded subsonic region thus necessitating the use of a three-dimensional, real-gas, time-dependent Navier-Stokes code. The time-dependent blunt-body code developed by Kutler et al.,[32] and later modified by Rizk et al.,[33] is used to obtain the blunt-nose solution and the initial data surface for the PNS code. The blunt-body code was modified in the present study to permit real-gas (equilibrium-air) calculations. The modifications are explained briefly here. At the shock, the pressure required to "fit" the shock is obtained by explicit integration of the combination of the continuity and energy equations. This pressure is used in conjunction with the approximate curve fit or table look-up procedure (previously discussed) to iteratively determine the shock speed. The rest of the procedure is identical to that given in Ref. 32. At the wall, the no-slip condition, the specified wall temperature, and the assumed zero normal pressure gradient are used in conjunction with the equilibrium-air curve fits to determine the density. The geometric singularity and outflow boundary conditions are independent of the gas model and were not modified. The new blunt-body code permits the user to specify either an ideal-gas ($\gamma = \text{const}$) or equilibrium-air model.

Results

The real-gas PNS code has been used to compute the laminar flow of an ideal gas ($\gamma = 1.2$) and equilibrium air around the forebody of the Orbiter. The flow conditions chosen for the computation correspond to the flight conditions at one point of the STS-3 trajectory ($t = 595$ s after reentry), where the altitude and velocity were 71.32 km and 6.74 km/s, respectively. The corresponding flow conditions[34,35] are shown in Table 1.

For these flow conditions, the blunt-body code was used to obtain the blunt-nose solution with the ideal-gas option ($\gamma = 1.2$). A $31 \times 31 \times 21$ grid was used in the computation. With this converged solution as a starting solution, the equilibrium-air blunt-nose solution was obtained for the same grid size. Figure 2 shows the shock shapes and sonic lines for both the ideal-gas and equilibrium-air computations. It is evident from the figure that the equilibrium-air shock-layer thickness differs from that of the $\gamma = 1.2$ calculation by only a small amount. The sonic lines do not show any discernible difference in their locations except near the stagnation region. Figure 3 shows the Mach contours for equilibrium air. As in the previous study,[18] both the ideal-gas and equilibrium-air blunt-nose solutions were obtained in a wind-axis coordinate system. The initial data surfaces required by the PNS code for

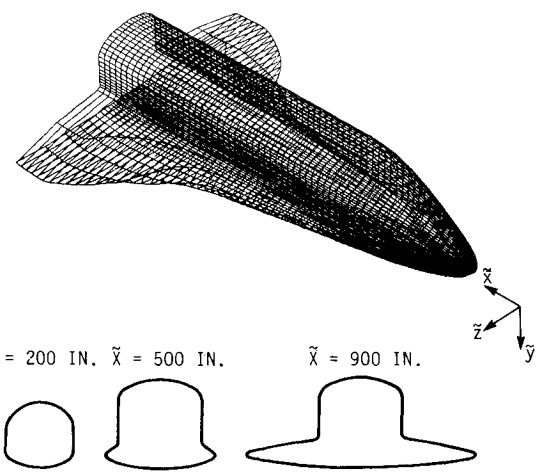

Fig. 1 Space Shuttle Orbiter geometry.

Table 1 Flow conditions

Quantity	Ideal gas	Equilibrium air
M_∞	20.985	20.985
α, deg	40.046	40.046
Re_L, $\times 10^6$	0.8816	0.8816
γ_∞	1.20	1.40
Pr_∞	0.72	0.72
$\tilde{T}_\infty$, K	256.690	256.690
$\tilde{p}_\infty$, N/m^2	5.1915	4.8057
$\tilde{\rho}_\infty$, kg/m^3, 10^{-5}	7.0460	6.5242
$\tilde{T}_w$, K	1100	1100

both the ideal-gas ($\gamma = 1.2$) and equilibrium-air calculations were chosen well away from the subsonic region. These data surfaces were slowly transformed into surfaces normal to the body axis as the computation proceeded downstream. The solution surfaces became x-axis normal at $\tilde{x}/\tilde{L} = 0.1$ and 0.15 for the ideal-gas and equilibrium-air cases, respectively. In addition, grid points were added as the computation proceeded downstream. Final grid sizes of 75×75 and 75×45 were used in the ideal-gas and equilibrium-air computations, respectively. Figure 4 shows a typical grid used in the calculation. As a first approximation, $\tilde{\gamma}$, μ, β, and k were assumed to be locally constant during each step in the equilibrium-air calculations. With this approximation, derivatives of the type $(\partial\tilde{\gamma}/\partial\tilde{e})_{\tilde{\rho}}$, $(\partial\tilde{\mu}/\partial\tilde{e})_{\tilde{\rho}}$, $(\partial\tilde{k}/\partial\tilde{e})_{\tilde{\rho}}$, $(\partial\tilde{\mu}/\partial\tilde{\rho})_{\tilde{e}}$, $(\partial\tilde{k}/\partial\tilde{\rho})_{\tilde{e}}$, etc., become zero, and the Jacobians given in Ref. 30 are simplified considerably.

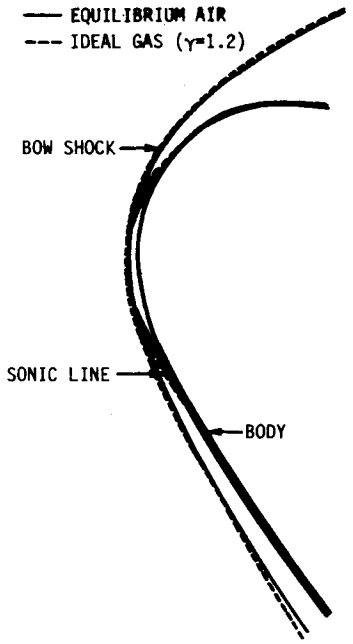

Fig. 2 Shock shape and sonic line location in the blunt-nose region.

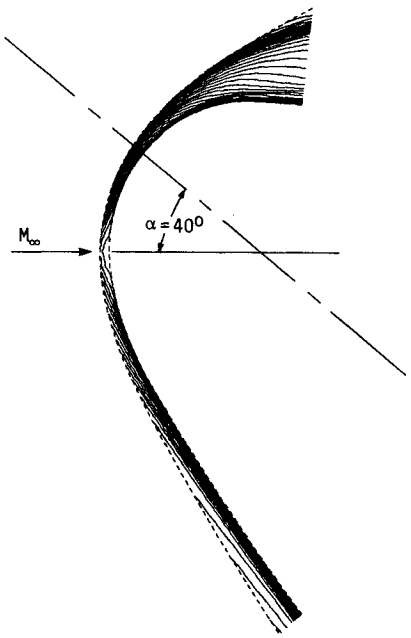

Fig. 3 Mach contours in the blunt-nose region (equilibrium air).

Solutions were obtained up to $\tilde{x}/\tilde{L} = 0.5$ and 0.405 for the ideal-gas and equilibrium-air cases, respectively. Numerical difficulties near the wing-body juncture prevented the solutions from being marched further downstream. These difficulties are believed to be the result of the algebraic grid generator which utilizes straight rays for the η coordinate lines as seen in Fig. 4.

Figure 5 shows the computed shock shapes for both cases. The shock shapes are nearly indistinguishable. Using an effective γ equal to 1.2 seems to model the shock standoff distance of equilibrium air quite closely. Figure 6 illustrates the comparison of computed windside wall pressures with STS-3 data. The computed pressures for both the ideal-gas and equilibrium-air cases are in good agreement with the flight data. Figure 7 shows a comparison between the computed leeside wall pressures and STS-3 data. The ideal-gas and equilibrium-air results are in fairly close agreement with each

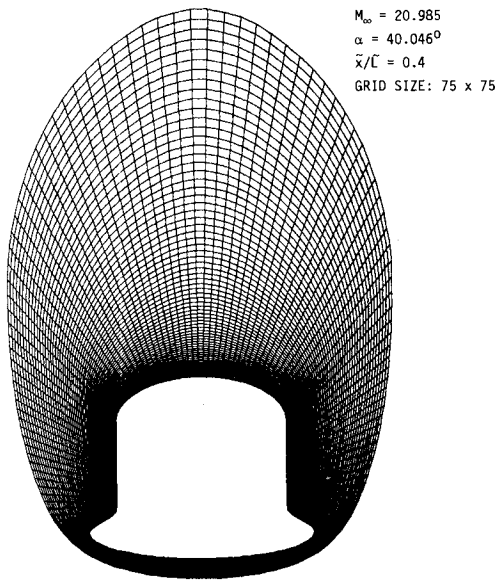

Fig. 4 Typical grid used in the PNS computations.

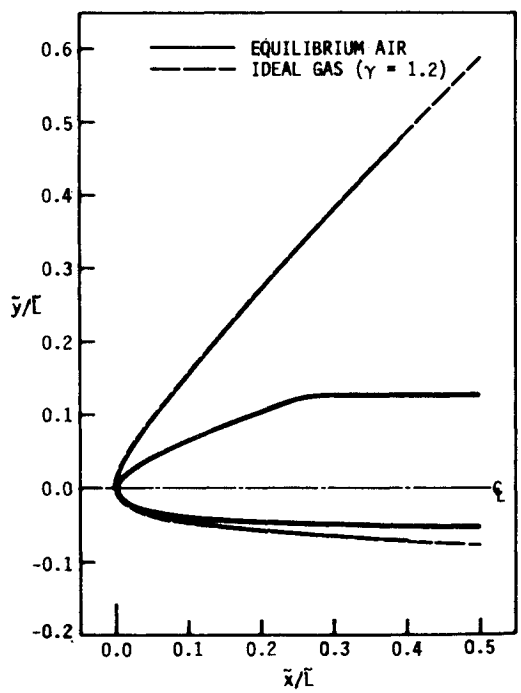

Fig. 5 Shock shape comparison.

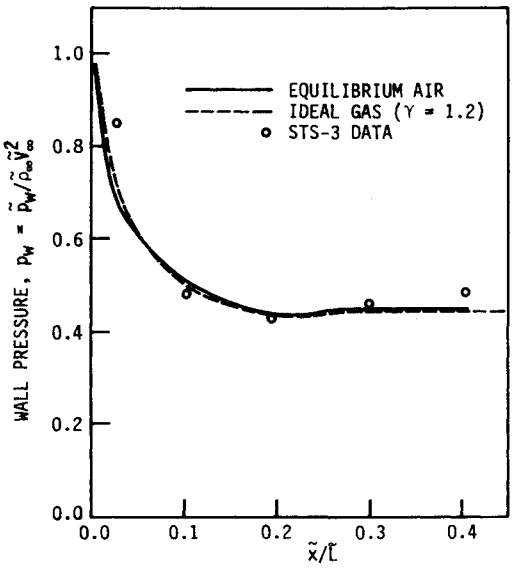

Fig. 6 Comparison of windside wall pressure.

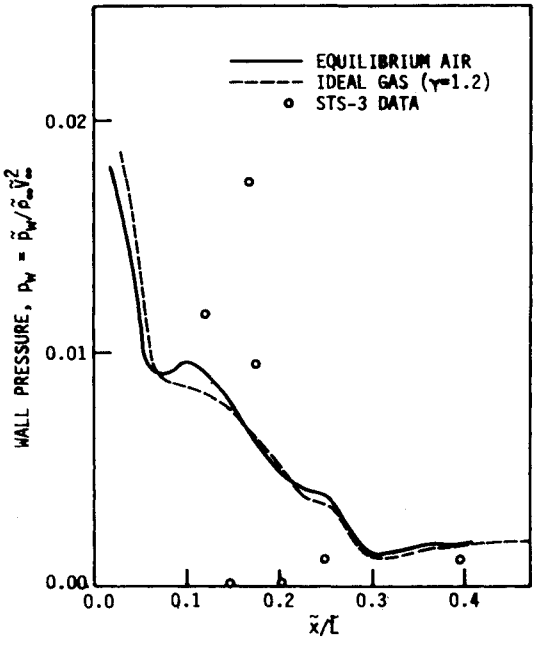

Fig. 7 Comparison of leeside wall pressure.

other, but not with the flight data. The flight data show a scatter in the canopy area. It should be mentioned again that the present Orbiter geometry does not include the canopy. Figures 8 and 9 show the comparison of computed wall pressures with STS-3 data at $\tilde{x}/\tilde{L}=0.1$ and 0.403, respectively. The ideal-gas ($\gamma=1.2$) and equilibrium-air calculations match each other fairly closely and both show reasonably good agreement with flight data.

The wall heating rates on the windward centerline are compared with flight data in Fig. 10. The equilibrium heating rates agree closely with the flight data beyond $\tilde{x}/\tilde{L}=0.2$. For the STS-3 flight, catalytic tiles were placed on the windward centerline at axial locations $\tilde{x}/\tilde{L}=0.3$ and 0.4.[34] The high heat transfer due to these tiles is clearly seen in Fig. 10. In Fig. 11 the computed leeside heating rates are compared with flight data. The heating rates are in good agreement with flight data except near the canopy. Figures 12 and 13 show the comparison of the computed wall heating rates with STS-3 data at $\tilde{x}/\tilde{L}=0.1$ and 0.403, respectively. The present equilibrium calculation overpredicts the heat transfer at $\tilde{x}/\tilde{L}=0.1$, but

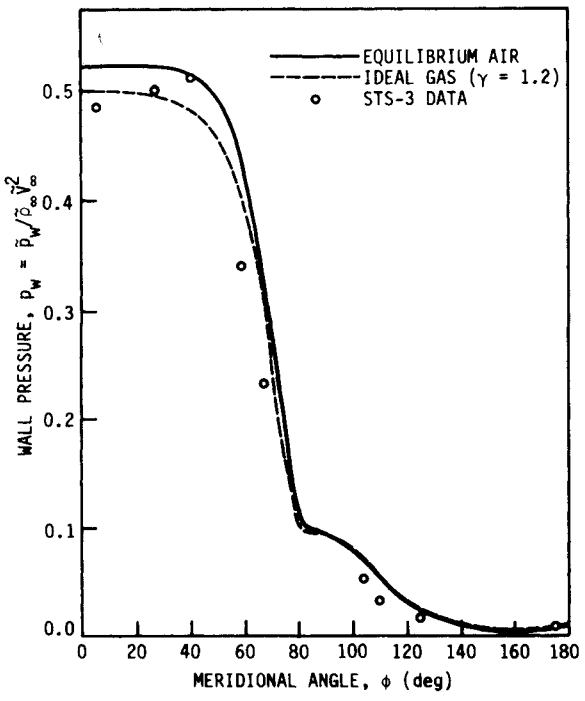

Fig. 8 Wall pressure comparison at $\tilde{x}/\tilde{L}=0.1$.

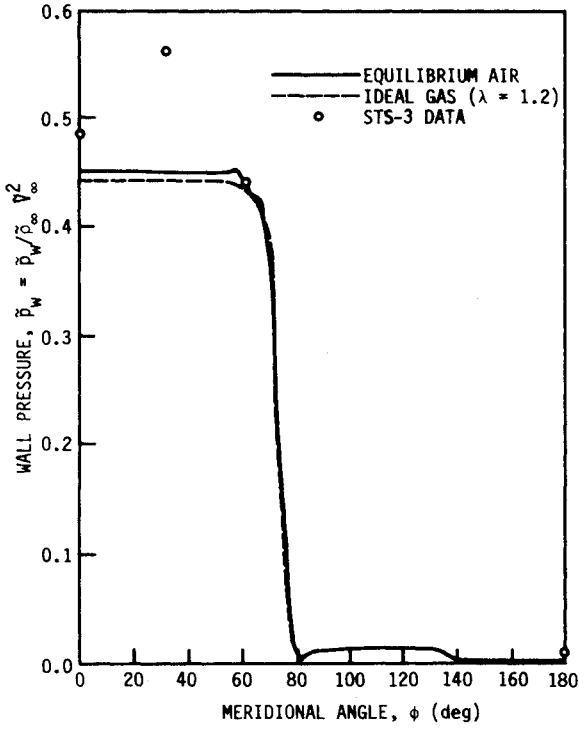

Fig. 9 Wall pressure comparison at $\tilde{x}/\tilde{L}=0.403$.

gives good agreement at $\tilde{x}/L=0.403$. In the present computations the wall temperature has been assumed to be constant at 1100 K throughout, while in the actual flight case the wall temperatures can vary from as high as 1400 K on the windside to as low as 250 K on the leeside.

The cross-flow velocity vectors at $\tilde{x}/\tilde{L}=0.403$ for the ideal-gas and equilibrium-air computations are compared in Figs. 14 and 15. These plots show the existence of the vortices on the leeside and at the wing-body juncture. Figures 16 and 17 show the Mach contours at the same axial location for ideal and equilibrium air, respectively.

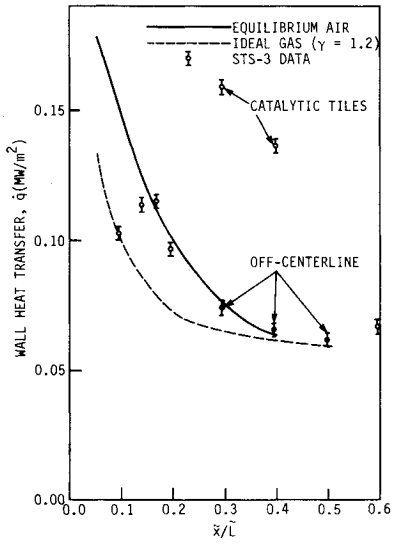

Fig. 10 Windside wall heat-transfer comparison.

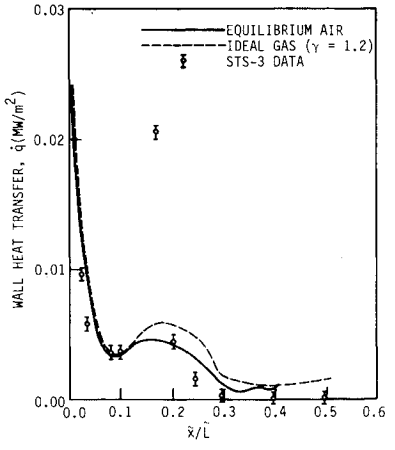

Fig. 11 Leeside wall heat-transfer comparison.

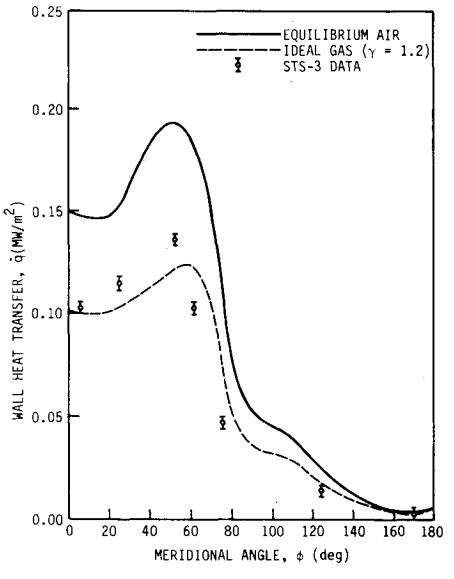

Fig. 12 Heat transfer comparison at $\tilde{x}/\tilde{L} = 0.1$.

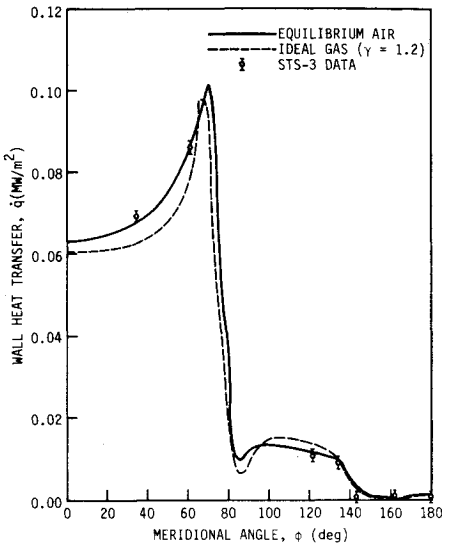

Fig. 13 Heat transfer comparison at $\tilde{x}/\tilde{L} = 0.403$.

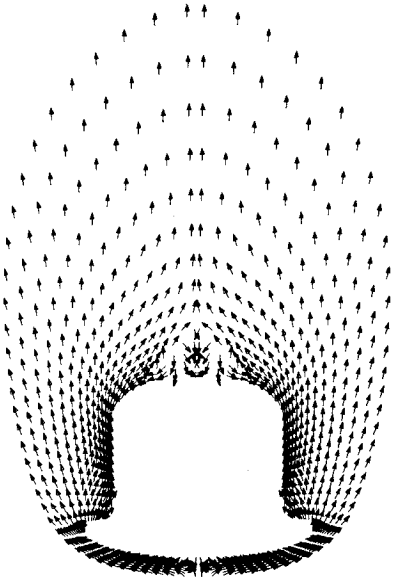

Fig. 14 Cross-flow velocity vector directions (ideal gas) at $\tilde{x}/\tilde{L} = 0.4$. $M_\infty = 20.985$, $\alpha = 40.046$ deg.

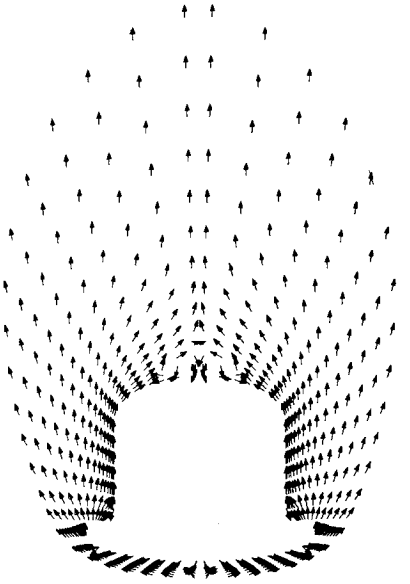

Fig. 15 Cross-flow velocity vector directions (equilibrium air) at $\tilde{x}/\tilde{L} = 0.4$. $M_\infty = 20.985$, $\alpha = 40.046$ deg.

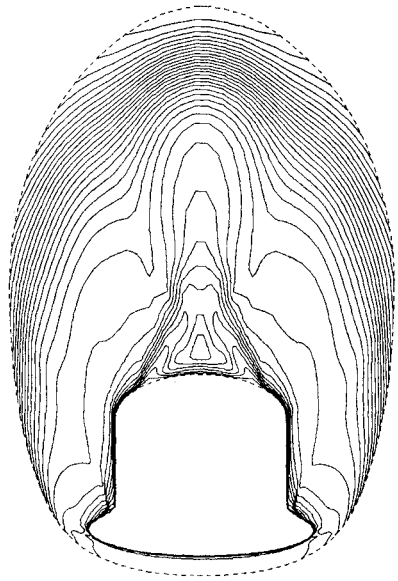

Fig. 16 Mach contours (ideal gas) at $\tilde{x}/\tilde{L}=0.4$. $M_\infty=20.985$, $\alpha=40.046$ deg.

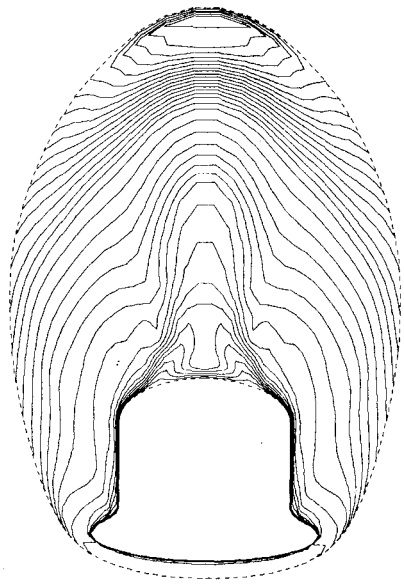

Fig. 17 Mach contours (equilibrium air) at $\tilde{x}/\tilde{L}=0.4$. $M_\infty=20.985$, $\alpha=40.046$ deg.

All of the present results were obtained using the CRAY X-MP computer at NASA Ames Research Center. The PNS code required 0.3×10^{-3} s/grid point/step for the ideal-gas calculation, 1.1×10^{-3} s/grid point/step for equilibrium-air calculations using approximate curve fits, and 1.8×10^{-3} s/grid point/step using the table look-up procedure. The blunt-body code required 0.27 and 0.73×10^{-3} s/grid point/step for the ideal-gas and equilibrium-air cases, respectively. Both the PNS and blunt-body codes are not vectorized. The blunt-body code required 2000 steps to converge the ideal-gas solution and 2500 additional steps to obtain an equilibrium-air solution. On the other hand, the PNS code took 1200 steps for both the ideal-gas and equilibrium-air computations.

Concluding Remarks

A real-gas parabolized Navier-Stokes (PNS) code has been used to compute both ideal-gas ($\gamma=1.2$) and equilibrium-air flow around the forebody of the Space Shuttle Orbiter. The "effective γ" and equilibrium-air approaches have yielded surface pressures that are in good agreement with each other and with the flight data. The heating rates were initially overpredicted by the equlibrium calculation, but good agreement was achieved as the solution proceeded downstream. The ability of the PNS code to predict the complex flowfield on the leeside and at the wing-body juncture is also clearly demonstrated.

Acknowledgments

This work was supported by NASA Ames Research Center under Grants NGR 16-002-038 and NAG-2-245 and by the Computational Fluid Dynamics Center, Iowa State University, Ames, Iowa. The authors wish to acknowledge the guidance and inspiration provided by Joe G. Marvin and the late John V. Rakich, who served as technical monitors for this project.

References

[1]Rakich, J.V. and Kutler, P., "Comparison of Characteristics and Shock Capturing Methods with Applications to the Space Shuttle Vehicle," AIAA Paper 72-191, Jan. 1972.

[2]Kutler, P., Lomax, H., and Warming, R.F., "Computation of Space Shuttle Flow Fields Using Noncentered Finite-Difference Schemes," *AIAA Journal,* Vol. 11, Feb. 1973, pp. 196-204.

[3]Kutler, P., Reinhardt, W.A., and Warming, R.F., "Multishocked Three-Dimensional Supersonic Flow Fields with Real Gas Effects," *AIAA Journal,* Vol. 11, May 1973, pp. 657-664.

[4]Weilmuenster, K.J. and Hamilton, H.H. II, "A Comparison of Computed Space Shuttle Orbiter Surface Pressures with Flight Measurements," AIAA Paper 82-0937, June 1982.

[5]Weilmuenster, K.J. and Hamilton, H.H. II, "Calculations of Inviscid Flow Over Shuttle-like Vehicles at High Angles of Attack and Comparisons with Experimental Data," NASA TP-2103, May 1983.

[6]Adams, J.C. Jr., Martindale, W.R., Mayne, A.W. Jr., and Marchand, E.O., "Real Gas Scale Effects on Hypersonic Laminar Boundary-Layer Parameters Including Effects of Entropy-Layer Swallowing," AIAA Paper 76-358, July 1976.

[7]Rakich, J.V. and Lanfranco, M.J., "Numerical Computation of Space Shuttle Laminar Heating and Surface Streamlines," *Journal of Spacecraft and Rockets,* Vol. 14, May 1977, pp. 265-272.

[8]Goodrich, W.D., Li, C.P., Houston, C.K., Chiu, P., and Olmedo, L., "Numerical Computations of Orbiter Flow Fields and Laminar Heating Rates," *Journal of Spacecraft and Rockets,* Vol. 14, May 1977, pp. 257-264.

[9]Zoby, E.V., "Approximate Heating Analysis for the Windward-Symmetry Plane of Shuttle-like Bodies at a Large Angle of Attack," AIAA Paper 81-1042, June 1981.

[10]Hamilton, H.H. II, "Approximate Method of Predicting Heating on the Windward Side of Space Shuttle Orbiter and Comparisons with Flight Data," AIAA Paper 82-0823, June 1982.

[11]Thareja, R., Szema, K.Y., and Lewis, C.H., "Viscous Shock-Layer Predictions for Hypersonic Laminar or Turbulent Flows in Chemical Equilibrium over the Windward Surface of a Shuttle-like Vehicle," AIAA Paper 82-0201, Jan. 1982.

[12]Shinn, J.L., Moss, J.N., and Simmonds, A.L., "Viscous-Shock-Layer Heating Analysis for the Shuttle Windward Plane with Surface Finite Catalytic Recombination Rate," AIAA Paper 82-0842, June 1982.

[13]Gupta, R.N., Moss, J.N., Simmonds, A.L., Shinn, J.L., and Zoby, E.V., "Space Shuttle Heating Analysis with Varation in Angle of Attack and Surface Condition," AIAA Paper 83-0486, Jan. 1983.

[14]Kim, M.D., Swaminathan, S., and Lewis, C.H., "Three-Dimensional Nonequilibrium Flow over the Space Shuttle Orbiter," *Journal of Spacecraft and Rockets,* Vol. 21, Jan.-Feb. 1984, pp. 29-35.

[15]Kim, M.D., Bhutta, B.A., and Lewis, C.H.., "Three-Dimensional Effects Upon Real Gas Flows Past the Space Shuttle," AIAA Paper 84-0225, Jan. 1984.

[16]Szema, K.Y., Griffith, B.J., and Maus, J.R., "Laminar Viscous Flow Field Prediction of Shuttle-like Vehicle Aerodynamics," AIAA Paper 83-0211, Jan. 1983.

[17]Li, C.P., "Numerical Simulation of Re-entry Flow Around the Space Shuttle Orbiter Including Real Gas Effects," *Computers in Flow Predictions and Fluid Dynamics Experiments,* ASME, Nov. 1981, pp. 141-149.

[18]Rakich, J.V., Venkatapathy, E., Tannehill, J.C., and Prabhu, D., "Numerical Solution of Space Shuttle Orbiter Flow Field," *Journal of Spacecraft and Rockets,* Vol. 21, Jan. 1984, pp. 9-15.

[19]Chaussee, D.S., Rizk, Y.M., and Buning, P.G., "Viscous Computation of a Space Shuttle Flow Field," *Proceedings of the Ninth International Conference on Numerical Methods in Fluid Dynamics,* Springer-Verlag, Saclay, France, June 1984, pp. 148-153.

[20]Tannehill, J.C., Venkatapathy, E., and Rakich, J.V., "Numerical Solution of Supersonic Flow over Blunt Delta Wings," *AIAA Journal,* Vol. 20, Feb. 1982, pp. 203-210.

[21]Maus, J.R., Griffith, B.J., Szema, K.Y., and Best, J.T., "Hypersonic Mach Number and Real Gas Effects on Space Shuttle Orbiter Aerodynamics," *Journal of Spacecraft and Rockets,* Vol. 21, March 1984, pp. 136-141.

[22]Balakrishnan, A., Davy, W.C., and Lombard, C.K., "Real Gas Flowfields About Three-Dimensional Configurations," AIAA Paper 83-0581, Jan. 1983.

[23]Balakrishnan, A. and Davy, W.C., "Viscous Real Gas Flowfields About Three-Dimensional Configurations," AIAA Paper 83-1511, June 1983.

[24]Venkatapathy, E., "A Generalized Solution Technique for the Parabolized Navier-Stokes Equations," Ph.D. Dissertation, Iowa State University, Ames, Iowa, 1982.

[25]Tannehill, J.C. and Mohling, R.A., "Development of Equilibrium Air Computer Programs Suitable for Numerical Computation Using Time-Dependent or Shock-Capturing Methods," NASA CR-2134, 1972.

[26]Tannehill, J.C. and Mugge, P.H., "Improved Curve Fits for the Thermodynamic Properties of Equilibrium Air Suitable for Numerical Computation Using Time-Dependent or Shock-Capturing Methods," NASA CR-2470, 1974.

[27]Lomax, H. and Inouye, M., "Numerical Analysis of Flow Properties About Blunt Bodies Moving at Supersonic Speeds in an Equilibrium Gas," NASA TR R-204, 1964.

[28]Vigneron, Y.C., "Hypersonic Viscous Flow of Equilibrium Air Around a Blunt Body," M.S. Thesis, Iowa State University, Ames, Iowa, 1976.

[29]Vigneron, Y.C., Rakich, J.V., and Tannehill, J.C., "Calculation of Supersonic Viscous Flow over Delta Wings with Sharp Subsonic Leading Edges," AIAA Paper 78-1137, July 1978.

[30]Prabhu, D.K. and Tannehill, J.C., "Numerical Solution of Space Shuttle Orbiter Flow Field Including Real Gas Effects," AIAA Paper 84-1747, June 1984.

[31]Thomas, P.D., Vinokur, M., Bastianon, R.A., and Conti, R.J., "Numerical Solution for Three-Dimensional Inviscid Supersonic Flows," *AIAA Journal,* Vol. 10, July 1972, pp. 887-894.

[32]Kutler, P., Pedelty, J.A., and Pulliam, T.H., "Supersonic Flow over Three-Dimensional Ablated Nosetips Using an Unsteady Implicit Numerical Procedure," AIAA Paper 80-0063, Jan. 1980.

[33]Rizk, Y.M., Chaussee, D.S., and McRae, D.S., "Computation of Hypersonic Viscous Flow Around Three-Dimensional Bodies at High Angles of Attack," AIAA Paper 81-1261, June 1981.

[34]Throckmorton, D.A., Hamilton, H.H. II, and Zoby, E.V., "Preliminary Analysis of STS-3 Entry Heat-Transfer Data for the Orbiter Windward Centerline," NASA TM-84500, June 1982.

[35]Throckmorton, D.A. and Zoby, E.V., "Orbiter Entry Leeside Heat Transfer Data Analysis," AIAA Paper 83-0484, Jan. 1983.